

PIMRL: PHYSICS-INFORMED MULTI-SCALE RECURRENT LEARNING FOR SPATIOTEMPORAL PREDICTION

Anonymous authors

Paper under double-blind review

ABSTRACT

Simulation of spatiotemporal systems governed by partial differential equations is widely applied in fields such as biology, chemistry, aerospace dynamics, and meteorology. Traditional numerical methods incur high computational costs due to the requirement of small time steps for accurate predictions. While machine learning has reduced these costs, long-term predictions remain challenged by error accumulation, particularly in scenarios with insufficient data or varying time scales, where stability and accuracy are compromised. Existing methods often neglect the effective utilization of multi-scale data, leading to suboptimal robustness in predictions. To address these issues, we propose a novel multi-scale learning framework, namely, the Physics-Informed Multi-Scale Recurrent Learning (PIMRL), to effectively leverage multi-scale data for spatiotemporal dynamics prediction. The PIMRL framework comprises two modules: the micro-scale module embeds physical knowledge into neural networks via pretraining, and the macro-scale module adopts a data-driven approach to learn the temporal evolution of physics in the latent space. Experimental results demonstrate that the PIMRL framework consistently achieves state-of-the-art performance across five benchmark datasets ranging from one to three dimensions, showing average improvements of over 9% in both RMSE and MAE evaluation metrics, with maximum enhancements reaching up to 80%.

1 INTRODUCTION

In the field of natural sciences, physical systems governed by partial differential equations (PDEs) have found widespread applications across disciplines including biology, chemistry, meteorology, etc. (Anderson & Wendt, 1995; Blazek, 2015; Moukalled et al., 2016; Karniadakis & Sherwin, 2005; Zienkiewicz et al., 2005). Although numerical methods have been regarded as reliable tools for modeling these systems, the use of Direct Numerical Simulation (DNS) faces significant hurdles due to inherent limitations. DNS necessitates high spatial resolution and fine time stepping, resulting in considerable computational demands and prolonged processing times. A case in point is the simulation of aerodynamic flows around aircraft, which typically requires the generation of millions of grid points, thereby imposing prohibitive computational requirements (Ahmad, 2013; Goc et al., 2021). Moreover, these numerical simulation methods require complete physical prior knowledge, such as PDE formula, parameters, and initial/boundary conditions (Ferziger et al., 2019).

The ongoing development of artificial intelligence (AI) has propelled research into data-driven simulation methods, showcasing significant potential (Lu et al., 2021; Li et al., 2020; Stachenfeld et al., 2021). These methods, which do not require prior physics knowledge, offer user-friendly solutions. They also overcome traditional constraints on resolution and small time stepping, ensuring accurate solutions. Nevertheless, when faced with sparse data and multi-scale temporal challenges, these methods often struggle to optimally utilize data. They may either discard micro-scale data in favor of macro-scale data or vice versa, leading to compromised accuracy.

Multi-scale Burst sampling is a technique capturing multiple samples at a high rate over a short period of time to record rapidly changing events or transient phenomena, e.g., fast dynamics, followed by a low sampling rate to capture slow dynamics (see Figure 1). Compared to traditional continuous sampling methods, it provides high-resolution data at critical moments while maintaining resource efficiency. But conventional uniform-scale models struggle to fully utilize such data. The latent

ODE approach (Rubanova et al., 2019) may work for multi-scale sampled data, but remains unclear whether it can address PDE problems. There is an urgent need for a new method to handle such a type of data for spatiotemporal systems.

Data-driven methods face significant limitations when addressing challenges related to insufficient data and multiple time scales mentioned above. To overcome these obstacles, current approaches integrate physical knowledge into the model learning process. Specifically, physics-informed neural networks (PINNs) (Raissi et al., 2019a; 2020; 2019b) design initial and boundary conditions as penalty terms in the loss function, thereby leveraging physical laws in a “soft” way. However, this soft embedding approach can sometimes lead to unsatisfactory results. To some extent, the embedding methods used in PINNs are unable to ensure that the model fully adheres to the embedded physical conditions.

Directly embedding physical equations into the model architecture, as seen in the physics-encoded recurrent convolutional neural network (PeRCNN) (Rao et al., 2023), ensures strict adherence to the underlying physical laws. This approach addresses the issue of soft constraints in PINNs and enhances the model’s interpretability and generalization capabilities. However, this approach requires continuous micro-scale data, which imposes stringent demands on the dataset and can introduce instability in long-term predictions. Alternatively, methods such as the learned interpolation (LI) model (Kochkov et al., 2021) and multiscale simulation frameworks (Vlachas et al., 2022) integrate numerical techniques with neural networks. These hybrid approaches enhance simulation efficiency while maintaining acceptable accuracy, although they still have some of the limitations inherent in traditional numerical methods.

Moreover, we observe that the error increases along with the prediction horizon, a phenomenon that is widespread. Although existing efforts are predominantly placed on enhancing the model’s predictive capability, long-term prediction of spatiotemporal dynamics still suffers from error accumulation. Hence, properly controlling the accumulation of errors is becomes crucial. Based on this core idea, we are motivated to leverage comprehensive multi-scale data through a novel Physics-Informed Multi-Scale Recurrent Learning (PIMRL) framework to tackle the problems mentioned above. This framework consists of macro-scale and micro-scale modules. The micro-scale module, pretrained to learn the underlying physical laws, enhances the accuracy of simulations. The macro-scale module reduces the accumulation of errors by minimizing the number of rollout iterations for the micro-scale module, thereby enhancing long-term predictive performance. The main contributions of this paper are summarized as follows:

- We proposed a new PIMRL framework that effectively leverages information from multi-scale data for long-term spatiotemporal dynamics prediction. The concept of reducing the accumulation of errors is achieved through the integration of the macro-scale and micro-scale modules.
- We designed a novel message passing mechanism between micro- and macro-scale modules, which effectively transmits physical information, enhances the micro-module’s correction capability, and reduces the number of micro-scale rollout iterations through the macro-scale module.
- The PIMRL model achieved optimal performance in effectively predicting the duration of multiple different cases from fluid dynamics to physical systems, demonstrating its scalability and laying a solid foundation for more generalizable models in the future.

2 RELATED WORK

Simulation tasks often aim to solve partial differential equations (PDEs) accurately and efficiently. Previous researchers have developed numerical methods achieving high precision with many nodes and short time steps. To speed up simulations, deep learning techniques have evolved from apply-

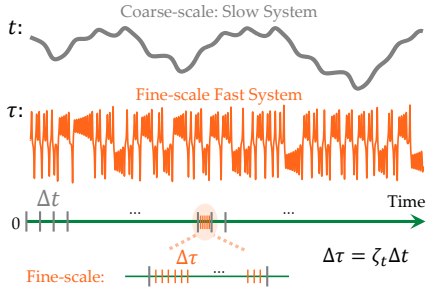


Figure 1: Multi-scale sampling, where $\Delta\tau$ denotes the micro-scale time interval for fast dynamics, Δt the macro-scale time interval for slow dynamics, and ζ_t the scale separation variable (typically $\zeta_t < 1$ or $\zeta_t \ll 1$).

ing conventional algorithms to designing new models that integrate physical knowledge, including hybrid methods and models embedding physical principles.

Computational fluid dynamics. Computational Fluid Dynamics (CFD) is a branch of fluid mechanics that uses numerical methods and algorithms to analyze and solve problems involving fluid flow (Anderson & Wendt, 1995; Blazek, 2015; Moukalled et al., 2016; Karniadakis & Sherwin, 2005; Zienkiewicz et al., 2005). When faced with complex problems, unacceptable time and computational costs are the primary obstacles limiting the application of CFD. Moreover, when the corresponding physical equations contain unknown parameters or even unknown terms, numerical methods are unable to perform accurate simulations. The aforementioned methods have inspired us to leverage physical knowledge. However, to overcome the aforementioned issues, we have decided to introduce deep learning methods into our PIMRL framework.

Deep learning methods. With the advancement of AI, the application of AI in physical system simulation tasks has become more diverse and profound. For example, classical convolutional neural network models (Stachenfeld et al., 2021; Bar-Sinai et al., 2019) and ResNet (Lu et al., 2018), U-Net (Gupta & Brandstetter, 2023) what originally used for image segmentation, graph neural networks (Sanchez-Gonzalez et al., 2020; Pfaff et al., 2020), and transformer-based models (Wu et al., 2024; Hang et al., 2024; Janny et al., 2023; Li et al., 2024) are now being employed. Neural operators used for learning mappings between function spaces have also seen significant development in physical simulation tasks, such as DeepONet (Lu et al., 2021), MWT (Gupta et al., 2021), FNO (Li et al., 2020; Tran et al., 2021; Rahman et al., 2022; Wen et al., 2022), etc. In addition, there are several methods specifically designed for spatiotemporal prediction tasks, such as ConvLSTM (Shi et al., 2015), PredRNN (Wang et al., 2022), and TrajGRU (Shi et al., 2017). The traditional deep learning methods mentioned above all require sufficient data for training; insufficient data can lead to poor model performance and severe overfitting issues. Moreover, error accumulation is another inevitable problem that limits the application of traditional deep learning methods. These limitations restrict the effectiveness and reliability of such models, especially in scenarios requiring long-term predictions or when data is scarce. The challenges outlined above have led us to propose a framework that effectively controls error accumulation and adeptly processes multi-scale data.

Physics-informed deep learning methods. To incorporate physical information into models, researchers have devised various methods. One category includes physics-inspired methods like PhyCRNet (Ren et al., 2022), PINN (Raissi et al., 2019a), and PhySR (Ren et al., 2023). Another category involves physical embedding methods, where explicit physics knowledge is embedded into the model to fully leverage physical principles, like EquNN (Wang et al., 2020) and PDE-Net (Long et al., 2018; 2019). PeRCNN (Rao et al., 2023; 2022) offers a “hard” encoding mechanism to learn the dynamics of physical systems from limited data. This approach leverages prior physics knowledge for predictions, thereby equipping strong predictive capabilities and robust generalization across different initial conditions. However, all the aforementioned methods suffer from error accumulation, making it difficult to obtain stable and accurate results in long-term prediction tasks. PeRCNN effectively utilizes physical information in a way that can be leveraged within PIMRL.

Hybrid learning methods. In recent years, an emerging research direction has been to integrate deep learning methods with traditional numerical methods. By combining classical solvers with deep neural networks, hybrid approaches designed on this principle can achieve acceptable accuracy while operating faster than pure numerical methods. Examples include the Learned Interpolation (LI) model (Kochkov et al., 2021) and numerical discretization learning (Zhuang et al., 2021). However, in these hybrid methods, the numerical method component is not involved in the training process, and such approaches also require substantial amounts of data. The pioneering work multi-scale simulations of complex systems (Vlachas et al., 2022) employs a multi-scale framework for predictions, effectively reducing the required time and computational cost while maintaining good accuracy. However, this method still requires ample data for training. The idea behind hybrid learning methods is very promising, so we have introduced our own message-passing mechanism within our PIMRL framework.

3 METHODOLOGY

We propose the PIMRL framework, as illustrated in Figure 2, for spatiotemporal dynamics prediction with a small amount of multi-scale training data

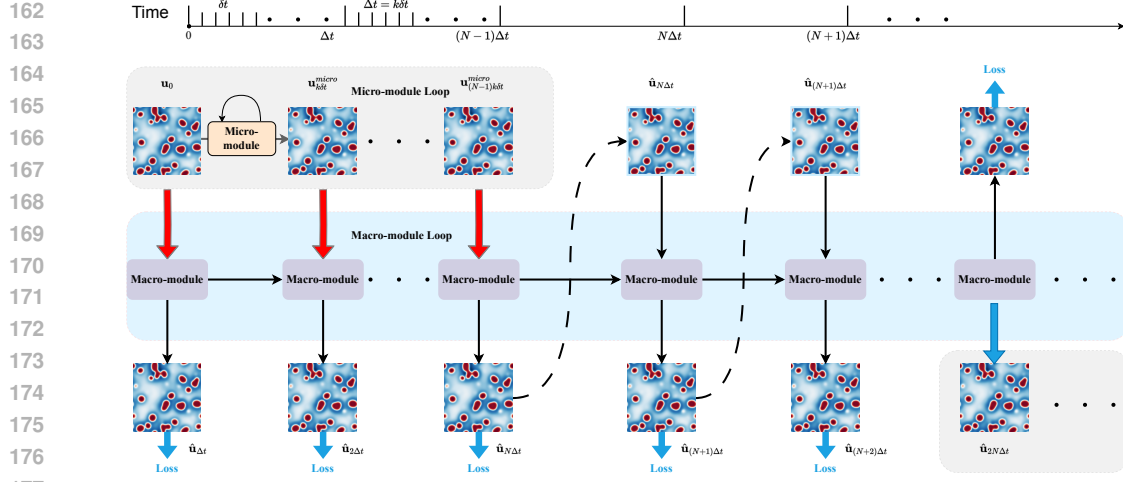


Figure 2: The overall framework architecture, which integrates physics-informed constraints with deep learning. The initial state of the system is denoted by \mathbf{u}_0 . The state predicted by the micro-module after k iterations, where each iteration occurs at intervals of δt , is represented by $\mathbf{u}_{k\delta t}^{micro}$. The predicted value of the physical state from PIMRL is denoted by $\hat{\mathbf{u}}$.

3.1 PARTIAL DIFFERENTIAL EQUATIONS SIMULATION TASK

Simulation tasks are intimately connected with PDEs, which are essential for describing and simulating physical models, and the time-dependent PDEs are defined as:

$$\mathbf{u}_t = \mathcal{F}(t, x, \mathbf{u}, \nabla \mathbf{u}, \mathbf{u} \cdot \nabla \mathbf{u}, \nabla^2 \mathbf{u}, \dots; \mu), \quad (1)$$

where $\mathbf{u}(x, t)$ denotes the spatiotemporal solution field, \mathbf{u}_t the first-order time derivative, $\mathcal{F}(\cdot)$ a linear/nonlinear function, ∇ the Nabla operator, ∇^2 the Laplace operator, and μ the PDE parameter.

In addition, we define the initial and boundary conditions (ICs, BCs) for this equation, namely: $I[\mathbf{u}](x, t = 0) = 0$ and $B[\mathbf{u}](x, t) = 0$ where I and B indicate IC and BC operators.

3.2 OVERVIEW

As outlined in the introduction, we have designed the PIMRL framework to mitigate error accumulation while ensuring that it can effectively capture the intrinsic changes in the physical system, rather than disregarding the physical information over large time intervals. Additionally, PIMRL is capable of efficiently utilizing multi-scale data. Below, we will provide a detailed exposition of the PIMRL framework’s architecture, the corresponding training methodologies, the macro and micro modules, as well as the boundary padding method that incorporates boundary conditions.

3.3 FORECASTING ARCHITECTURE

As shown in Figure 2, the PIMRL framework comprises two key components: the micro-scale module and the macro-scale module. The message-passing mechanism is an interaction between the micro-module and the macro-module. The information transmitted includes physical knowledge learned by the micro-module and corrections applied to the macro-module. Additionally, the macro-module also passes information to future iterations of the micro-module.

PIMRL is designed to achieve long-term prediction of spatiotemporal dynamics. PIMRL operates in a recursive manner, involving cycles at the micro-module level, the macro-module level, and the overall framework level. Only the output from the macro-module contributes to the final output of the PIMRL framework and is used to compute the loss for training the entire framework, whereas the output from the micro-module serves as intermediate variables within the framework. And the message-passing mechanism is described as follows:

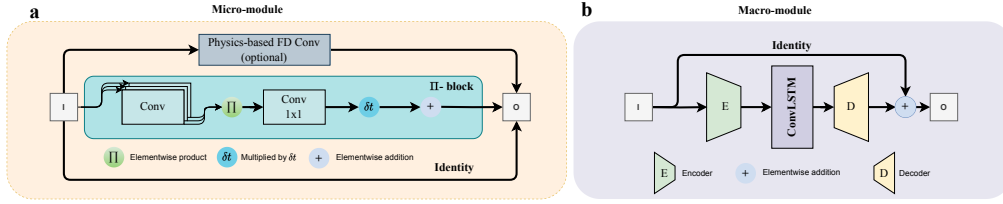


Figure 3: PIMRL includes two main modules: (a) the micro-module, designed to capture local features and small-scale dynamics; and (b) the macro-module, which captures long-term dependencies and global patterns using residual connections.

- Firstly, the micro-module loop is a simple autoregressive process with time step δt , where the output at the previous time step serves as the input for the next time step. Secondly, the macro-module loop performs self-cycles.
- When the micro-module is involved in the prediction, for every k steps of micro-module with δt like Equation 3, the final output of micro-module is passed to the macro-module, and at this point, the output from the macro-module serves as the output of the entire PIMRL model shown as Equation 4. When the micro-module is not involved in the prediction, the macro-module loop is a simple autoregressive process with time step Δt .
- Finally, there is a PIMRL loop that operates in conjunction with the macro-module loop. After every $N - 1$ cycles of the macro-module loops, the micro-module stops participating in the prediction, and the macro-module performs N steps of autoregressive prediction on its own. This completes a total of $2N$ cycles. Each output from the macro-module during these $2N$ cycles serves as the output of PIMRL as depicted in Equation 2.

We utilize two equations to represent the relationship between the micro-scale module and the macro-scale module, denoted as F_{micro} and F_{macro} respectively, as illustrated in Figure 2. The details of this process can be represented using the aforementioned symbols as follows:

$$\text{PIMRL Loop: } \hat{\mathbf{u}}_{t+2N\Delta t} = \underbrace{F_{macro}(\dots F_{macro}(\hat{\mathbf{u}}_{t+Nk\delta t}))}_{\times N}, \quad (2)$$

$$\text{Macro-module Loop: } \mathbf{u}_{k\delta t}^{micro} = \underbrace{F_{micro}(\dots F_{micro}(\mathbf{u}_t))}_{\times k}, \quad (3)$$

$$\text{Macro-module Loop: } \hat{\mathbf{u}}_{t+2k\delta t} = F_{macro}(\mathbf{u}_{k\delta t}^{micro}), \quad (4)$$

where the variable \mathbf{u} denotes the physical state. The relationship between the micro-time step δt and the macro-time step Δt is given by $\Delta t = k\delta t$, where k is an adjustable parameter determined by the time stepping of different scales in the real data.

3.4 TRAINING STRATEGIES

Since the PIMRL model consists of micro- and macro-scale modules, adopting brute-force end-to-end training yields unsatisfactory results (see the ablation study). Firstly, we establish a pre-training phase where only the micro-module is trained. The purpose of this pre-training phase is to enable the micro-module to effectively learn the dynamics of the physical system and the underlying physical laws, free from the influence of the macro-module. In the next phase, referred to as the overall training phase, all modules within the PIMRL framework are engaged in training together. During this phase, the micro-module benefits from the parameters pre-trained in the pre-training phase, serving to supervise and correct the macro-module. The output from the macro-module serves as the final output of the entire PIMRL framework and is used to compute the loss. The details are shown in Appendix C.1.

3.5 MICRO-SCALE MODULE

The micro-scale module is designed to learn **underlying** physical laws that govern the spatiotemporal dynamics from micro-scale data with small time stepping, where we adopt the PeRCNN model (Rao

et al., 2023) with the architecture of Π -block shown in Figure 3(a). In a forward Euler scheme: $\mathbf{u}_{(k+1)\delta t} = \hat{\mathcal{F}}(\mathbf{u}_{k\delta t}) \cdot \delta t + \mathbf{u}_{k\delta t}$, where δt denotes that the module predicting in micro-scale time stepping. We can then approximate the \mathcal{F} by $\hat{\mathcal{F}}$ described as follows:

$$\hat{\mathcal{F}}(\mathbf{u}_{k\delta t}) = \sum_{c=1}^{N_c} W_c \cdot \left[\prod_{N_l}^{l=1} (K_{c,l} \star \hat{\mathbf{u}}_{k\delta t} + b_l) \right]. \quad (5)$$

where N_c denotes the channel count, and N_l the total number of parallel convolutional layers. The symbol \star denotes the convolutional operation. For each layer l and channel c , $K_{c,l}$ designates the specific filter weight, while b_l stands for the bias term of that layer l . In the context of a 1×1 convolutional layer, W_c denotes the weight assigned to the c^{th} channel, with the bias term being omitted here for the sake of simplicity and brevity.

When a certain term in the governing PDE remains known (e.g., the diffusion term $\Delta \mathbf{u}$), its discretization can be directly embedded in PeRCNN (called the physics-based Conv layer as shown in Figure 3(a)). The convolutional kernel in such a layer can be set according to the corresponding finite difference (FD) stencil. In essence, the physics-based Conv connection is constructed to incorporate known physical principles, whereas the Π -block is aimed at capturing the complementary unknown dynamics. The details of the physics-based FD Conv are provided in Appendix B.

3.6 MACRO-SCALE MODULE

The design of the macro-scale module, as a pivotal component of the PIMRL framework, is meticulously crafted to effectively manage and analyze macro-scale data. This type of data often poses unique challenges due to the substantial time spans it encompasses, which in turn lead to significant variations in the underlying physical states captured within the data points. These variations might be highly nonlinear and dynamic, making it difficult for traditional, physically motivated modeling methods to accurately capture all the nuances and complexities involved. As depicted in Figure 3, our macro-scale module utilizes ConvLSTM block with a residual connection. The structure of each block, illustrated in Figure 3(b), consists of a pair of encoders and decoders, along with a ConvLSTM cell shown in Appendix Figure S3. The input to this block undergoes mapping by the encoder, where the feature map serves as the characteristic of the latent space. Following this, the ConvLSTM cell simulates the dynamics, and the output is mapped back to the physical space through the decoder. Finally, the output, as a residual, is added to the feature from the previous time step to generate the prediction for the next time step. More details are provided in Appendix C.1.

3.7 BOUNDARY CONDITION PADDING

Inspired by PeRCNN (Rao et al., 2023), we introduce BC hard encoding in both micro-scale and macro-scale modules. This encoding method ensures that the feature maps comply with the given BCs during the convolution process while also serving the purpose of padding, which involves filling the feature maps before convolution operations. Specifically, in this paper, our case adheres to periodic BCs, and the application of the corresponding padding is illustrated in Figure 4. This encoding scheme ingeniously incorporates BCs into the padding, thereby enhancing the accuracy of the prediction.

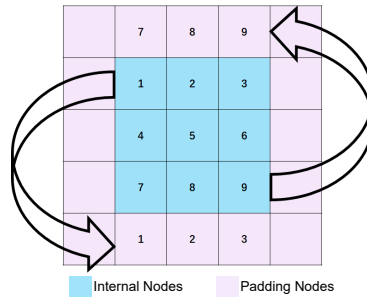
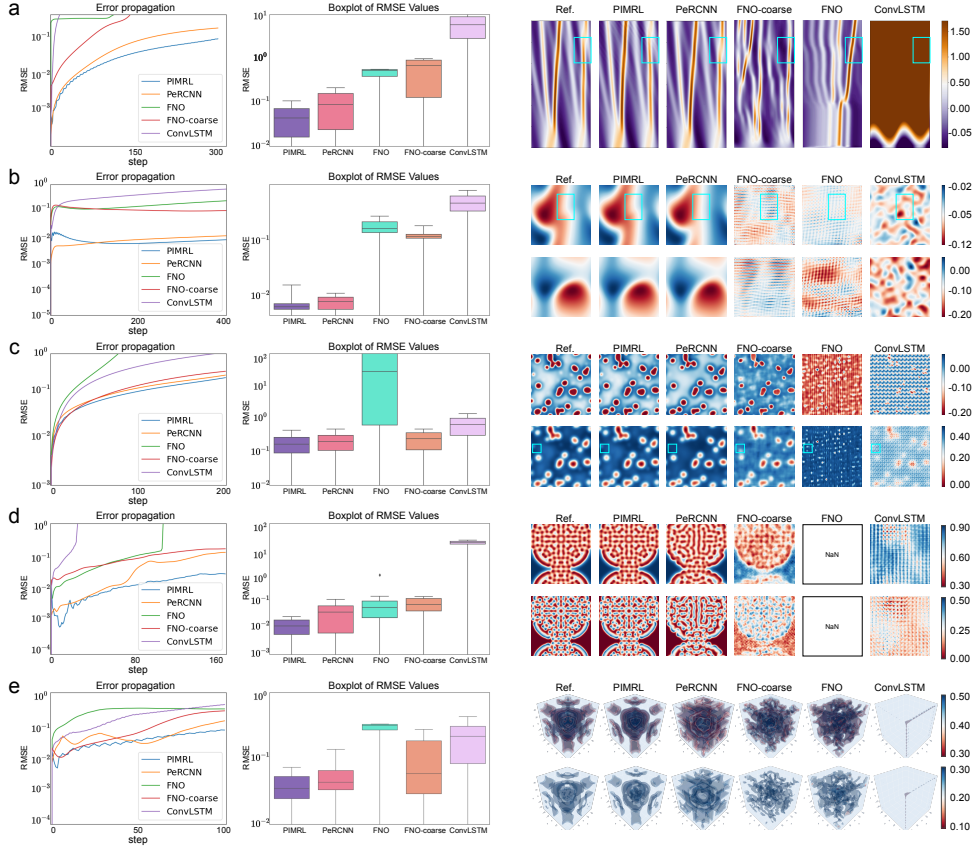


Figure 4: Periodic BC padding.

4 EXPERIMENTS

To validate the effectiveness and versatility of our proposed PIMRL framework, we conducted extensive experiments on a diverse set of fluid dynamics and reaction-diffusion systems equations. Specifically, we tested our model on the following cases: the 1D Korteweg-de Vries (KdV) equation, the 2D Burgers equation, and three reaction-diffusion (RD) equations. These equations represent a range of physical phenomena with varying degrees of complexity and nonlinearity. Our results show that PIMRL consistently outperforms existing methods in terms of accuracy and robustness across these challenging cases.

324
325
326
327
328
329
330
331
332
333
334
335
336
337
338
339
340
341
342
343
344
345
346
347
348
349
350
351
352



353 Figure 5: An overview of the comparison between our PIMRL framework and baseline models is
354 provided, including error propagation curves (left), error boxplots (middle), and final prediction plots
355 (right). Figures (a) through (e) respectively showcase the qualitative results for the KdV, Burgers,
356 2D GS, FN, and 3D GS cases.

357
358 **Datasets.** We conducted experiments on five datasets, including: Korteweg-de Vries (KdV), 2D
359 Burgers, FitzHugh-Nagumo (FN), 2D Gray-Scott (2D GS), and 3D Gray-Scott (3D GS). **The IC for the Kdv equation is created by summing multiple sine waves with random amplitudes, phases, and frequencies, resulting in a complex waveform. ICs for the Burgers' equation are generated randomly according to a Gaussian distribution. The FN equation is initialized with random Gaussian noise for a warm-up period, after which time sequences are extracted to form the dataset. The GS equation starts the reaction from random initial positions and then diffuses. In these cases, except for the Kdv case, which was solved using the Finite Volume Method (FVM), the rest were solved using the Finite Difference Method (FDM).** Additionally, We have two sets of data with different time scales originating from the same ICs. The micro-scale data $\mathbf{U}^{\text{micro}} = \{\mathbf{u}_0, \mathbf{u}_{\delta t}, \mathbf{u}_{2\delta t} \dots\} \in \mathbb{R}^{\text{micro}}$ is characterized by short and scattered continuous time intervals, while the macro-scale data $\mathbf{U}^{\text{macro}} = \{\mathbf{u}_0, \mathbf{u}_{\Delta t}, \mathbf{u}_{2\Delta t} \dots \mathbf{u}_{\text{Tend}}\} \in \mathbb{R}^{\text{macro}}$ exhibits persistent continuity until the end. The validation and test sets are established based on different ICs but with the same parameters, making it more challenging than extrapolation under the same ICs. The dataset configuration is presented in Appendix G.

372 **Model training.** The primary objective is to first pretrain the micro-scale module using the micro-
373 scale data to learn **the underlying physics**. Subsequently, the pretrained micro-scale module is
374 integrated into the overall framework, and the entire model is trained using macro-scale data to
375 capture the spatial evolution patterns over long time stepping. Both the pretraining and training
376 processes can be formulated as auto-regressive rollout problems. The loss function is defined as
377 $L(\theta) = \frac{1}{BN} \sum_{i=1}^B \sum_{j=1}^N (y_{i,j} - \hat{y}_{i,j})^2$, where the B and N denote the number of batches and the
batch size. The θ indicates all the trainable parameters and $(y_{i,j} - \hat{y}_{i,j})$ means the difference be-

tween the rollout-prediction $\hat{y}_{i,j}$ of j -th sample in the i -th batch and the corresponding labeled data $y_{i,j}$. More training details are shown in Appendix E.

Baseline models. To validate the effectiveness of the proposed PIMRL framework, we introduced several baseline models. Firstly, we considered the widely recognized high-performing data-driven model FNO (Li et al., 2020), which has been trained on datasets with two different time intervals, denoted as FNO (trained on fine-scale data with small time steps) and FNO-coarse (trained on coarse-scale data with large time steps). In particular, we examined the impact of cumulative error on long-term predictions. Our results show that the influence of error accumulation is significant. Detailed analysis is provided in Section 4.1. Secondly, we included the PeRCNN model (Rao et al., 2023), which embeds physical knowledge in a hard way and demonstrates excellent performance on multiple datasets. Due to constraints on the time stepping of the model, PeRCNN is trained only on datasets with small time stepping. Lastly, we incorporated ConvLSTM (Shi et al., 2015), a classic sequential prediction model trained on datasets with large time stepping, serving as the macro-scale module within our framework in a residual way. The details are shown in the Appendix E.

Evaluation Metrics. To comprehensively evaluate the performance of our model, we adopted several metrics: Root Mean Square Error (RMSE), Mean Absolute Error (MAE), and High Correction Time (HCT). These metrics provide a multi-faceted assessment of the model’s accuracy and reliability. RMSE is calculated on the macro-scale data to facilitate comparisons between models operating at different granularities. MAE provides a measure of the average absolute difference between the predicted and actual values, less sensitive to outliers compared to RMSE. HCT evaluates the time it takes for the model to correct its predictions to a high level of accuracy, which is particularly important for long-term prediction. Detailed formulas for these metrics are provided in Appendix F.

4.1 MAIN RESULTS

Figure 5 illustrates the performance results of our framework in comparison with various baseline models across different cases, including error propagation, showcasing box plots of different quantities and their prediction outcomes. Additionally, Table 1 presents relevant quantitative metrics as an expression of the results, where * in Table 1 indicates that the inference process has reached the end of the test data.

KdV Equation. The KdV equation describes the evolution of nonlinear wave phenomena. In this study, due to the absence of one-dimensional instances in the PeRCNN model, we designed our own physical embedding module and corresponding model, following the principles of PeRCNN as detailed in Appendix B. We observed significant discrepancies between the predictions of the PeRCNN model and the ground truth, as shown in the blue box of Figure 5(a). Meanwhile, the other baseline models performed poorly at the start, likely due to the complexity of the KdV equation. In contrast, our proposed model demonstrated substantial advantages over the baseline models in terms of predictive accuracy. It maintained a consistent basic shape with the ground truth values, even in long-term forecasts. As shown in Table 1, the PIMRL framework achieved 30% to 50% improvements in the evaluation metrics, highlighting a significant advancement in the field.

Table 1: Quantitative results of our model and baselines.

Case	Model	RMSE ↓	MAE ↓	HCT (s) ↑
KdV	ConvLSTM	5.8507	7.6036	9.6
	FNO	0.4891	0.3300	0.45
	FNO-coarse	0.5461	0.4167	7.8
	PeRCNN	<u>0.0942</u>	<u>0.0941</u>	<u>30</u>
	PIMRL(Ours)	0.0457	0.0607	46.2
	Promotion (↑)	51.5%	35.5%	54.0%
Burgers	ConvLSTM	0.4020	0.3232	0.176
	FNO	0.1561	0.1301	0.104
	FNO-coarse	0.1094	0.0879	0.064
	PeRCNN	<u>0.0075</u>	<u>0.0058</u>	<u>3.216</u>
	PIMRL(Ours)	0.0068	0.0049	3.216
	Promotion (↑)	9.3%	15.6%	0%*
FN	ConvLSTM	0.5077	0.4925	1.86
	FNO	937	2393980	1.65
	FNO-coarse	0.1878	0.1643	4.98
	PeRCNN	<u>0.1591</u>	<u>0.1139</u>	<u>6.99</u>
	PIMRL(Ours)	0.1349	0.0990	7.74
	Promotion (↑)	15.2%	13.1%	10.7%
2DGS	ConvLSTM	15.7559	13.7966	195
	FNO	NaN	NaN	810
	FNO-coarse	0.0884	0.0629	1335
	PeRCNN	<u>0.0455</u>	<u>0.0268</u>	<u>1379.5</u>
	PIMRL(Ours)	0.0133	0.0072	1965*
	Promotion (↑)	70.8%	73.1%	42.5%
3DGS	ConvLSTM	0.2081	0.2009	562.5
	FNO	0.2798	0.1950	112.5
	FNO-coarse	0.1042	0.0611	360
	PeRCNN	<u>0.0532</u>	<u>0.0977</u>	<u>510</u>
	PIMRL(Ours)	0.0381	0.0190	731.25
	Promotion (↑)	28.4%	80.6%	43.4%

2D Burgers Equation. On the right side of Figure 5(b), we observe that besides our framework, only PeRCNN achieved satisfactory results after training on the micro-scale, while the remaining baseline models failed to capture the physical changes effectively. Additionally, in the areas marked by the blue box in Figure 5(b), we can see errors in PeRCNN’s predictions for long-term forecasts, whereas our PIMRL framework demonstrates superior performance, as also visually depicted in Figure 5(b). In the error propagation shown in Figure 5(b), we notice that although initially our framework exhibits higher RMSE compared to the PeRCNN model due to the macro-scale module, the accumulated errors lead to inaccurate predictions by PeRCNN over time. While PeRCNN and PIMRL exhibit the same performance on the HCT metric, this similarity arises from insignificant changes in the later stages. The cumulative error of PeRCNN does not reflect in this particular metric. As shown in Table 1, there are significant improvements in both RMSE and MAE. Additionally, the noticeable divergence of PeRCNN can be observed in the snapshot of the final step.

2D FitzHugh-Nagumo Equation. In the Figure 5(c), we can observe that the purely data-driven method mentioned earlier fails to fully exhibit its original performance on this relatively small dataset. FNO and FNO-coarse represent the effectiveness of the FNO method when trained on datasets of different granularities, respectively. It is worth noting that the performance of FNO-coarse surpasses that of the FNO model trained on micro-scale data. This result effectively validates our hypothesis that error accumulation can significantly impact the model’s performance in long-term multi-step predictions. Quantitatively, our model has improved by at least 10% compared to the currently best-performing model. Furthermore, in the Table 1 we observe that the variation curves of RMSE and other metrics for our model and the PeRCNN model exhibit a striking similarity, yet our model outperforms PeRCNN. This not only indicates that PeRCNN effectively leverages its supervised refinement capabilities but also demonstrates its ability to mitigate the influence of cumulative errors through the evolution of larger time stepping.

2D Gray-Scott Equation. As shown in the left part of Figure 5(d), only PIMRL effectively carried out long-term predictions, showcasing a clear demonstration of the cumulative errors of PeRCNN in this case. The model exhibited significant deviations from ground truth values over extended periods, highlighting its limitations in capturing long-term variations. Among the other models, FNO-Coarse exhibited the best performance. It is evident that FNO performed poorly in the absence of physically informed embeddings, particularly with small time stepping. In this case, Table 1 further validates the superior performance of PIMRL with both RMSE and MAE showing an improvement of over 70%, and the HCT similarity of PIMRL still at 0.99 at the final prediction step. This underscores the effectiveness of the PIMRL framework in enhancing predictive accuracy and maintaining consistency in the predictions throughout the forecasting process. Such robust performance metrics highlight the potential of PIMRL in addressing complex data-driven challenges.

3D Gray-Scott Equation. As shown on the right side of Figure 5(e), the predictions under our framework closely align with the ground truth. Through box plots and error evolution graphs, it is evident that PeRCNN, as the best-performing model among the baselines in our study, outperformed the other models lacking physical knowledge embeddings, especially when compared to FNO trained on the same dataset. In quantitative analysis of Table 1, the improvements are also significant, not only in the overall evaluation metrics of RMSE and MAE in 28.4% and 80.6% but also in the substantial growth of the HCT in 43.4%.

4.2 ABLATION STUDY

Table 2: Results for ablation study.

Model	RMSE
PIMRL w/o Connect	0.1975
FNO-MRL	0.7854
PIMRL w/o Pretraining	0.2599
PIMRL w/o Physics-based FD Conv	0.1738
PeRCNN w/o Physics-based FD Conv	NaN

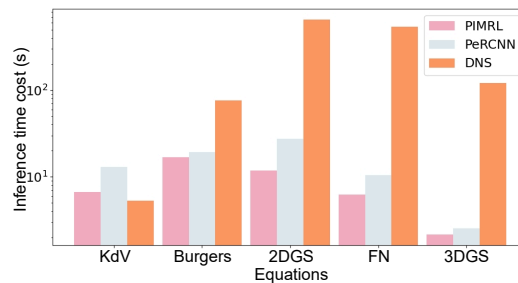
To evaluate the impact of components of PIMRL and demonstrate the effectiveness of our framework structure, we have designed five novel models and provided their RMSE results in the FN case. (1) The ablation study with the “PIMRL w/o Connect”, where the connections between the micro-module and the macro-module are removed, is designed to demonstrate the effectiveness of the PIMRL framework’s structural design. This experiment, which leaves only the serial structure of the two modules, shows that the connections within the PIMRL framework are essential for its performance. (2) The “FNO-MRL” replaces the micro-scale module containing physical information, PeRCNN, with the data-driven model FNO, aiming to validate the efficacy of the physical embedding in the micro-scale module

486 within our framework. (3) “PIMRL w/o Pretraining” provides a perspective on the training method
 487 by eliminating the pretraining step for the micro module. In this ablation study, the absence of
 488 pretraining leads to inferior performance compared to the PIMRL. This demonstrates that directly
 489 introducing large time intervals for training can deprive the micro module of the opportunity to learn
 490 fine-grained changes, similar to why PeRCNN cannot be directly used with large time intervals. (4)
 491 “PIMRL w/o Physics-based FD Conv” indicates the removal of the Physics-based FD Convolution.
 492 This ablation study emphasizes the effectiveness of the Physics-based FD Conv by showing the
 493 performance degradation when it is omitted. (5) “PeRCNN w/o Physics-based FD Conv” is a ver-
 494 sion of PeRCNN without the Physics-based Finite Difference (FD) Convolution. While this version
 495 can initially make relatively accurate predictions, the errors accumulate over subsequent iterations,
 496 eventually becoming unacceptably large.

497 The five ablation studies conducted not only validate the effectiveness of the interaction design by
 498 removing the connection mechanisms but also highlight the contribution of our proposed connection
 499 approach. Additionally, by substituting the micro-modules with non-physics-embedded data-driven
 500 models, the experiments confirm the efficacy of the physics-embedding within our PIMRL frame-
 501 work. Subsequent pre-training ablation experiments and the removal of the Physics-based FD Conv
 502 further substantiate the effectiveness of the corresponding methods and modules.

504 4.3 INFERENCE TIME

505 In the aforementioned cases, PIMRL not only
 506 achieves state-of-the-art performance in long-
 507 term predictions but also significantly reduces
 508 the computational time cost. Compared to
 509 traditional methods such as Direct Numerical
 510 Simulation (DNS), our framework is substan-
 511 tially faster, demonstrating a significant im-
 512 provement in computational efficiency (given
 513 the same computing facility, aka, CPU). Addi-
 514 tionally, PIMRL not only delivers superior pre-
 515 dictive accuracy, but also outperforms PeRCNN in terms of computational efficiency. The numerical
 516 methods used for DNS are consistent with the parameter settings during data generation. The differ-
 517 ence lies in the required prediction time length, which needs to be the same as that of PIMRL and
 518 PeRCNN for a fair comparison.



519 Figure 6: Computational time for comparison

520 5 CONCLUSIONS

521 This paper introduces a new multi-scale temporal model named Physics-Informed Multi-Scale Re-
 522 current Learning (PIMRL) for prediction of spatiotemporal dynamics. Adhering to the idea of con-
 523 trolling cumulative error by reducing iterations, PIMRL integrates modules across different scales
 524 within its framework to realize this concept, and it can efficiently leverage multi-scale data, which
 525 facilitates learning physical laws with limited resources. From fluid dynamics to reaction-diffusion
 526 systems, PIMRL demonstrates superior performance in handling multi-scale data, providing accu-
 527 rate long rollout predictions. Our future work will optimize the macro-scale model for time-series
 528 tasks to improve computational efficiency and predictive accuracy. We also plan to integrate super-
 529 resolution techniques to enhance the model’s adaptability to various spatiotemporal scales, broad-
 530 ening its application to more complex physical systems.

533 REFERENCES

- 534 Nashat N. Ahmad. Numerical simulation of the aircraft wake vortex flowfield. In *5th AIAA Atmo-
 535 spheric and Space Environments Conference*, pp. 2552, 2013.
- 536 John David Anderson and John Wendt. *Computational Fluid Dynamics*, volume 206. Springer,
 537 1995.

- 540 Yohai Bar-Sinai, Stephan Hoyer, Jason Hickey, and Michael P Brenner. Learning data-driven dis-
541 cretizations for partial differential equations. *Proceedings of the National Academy of Sciences*,
542 116(31):15344–15349, 2019.
- 543 Jiri Blazek. *Computational fluid dynamics: principles and applications*. Butterworth-Heinemann,
544 2015.
- 546 Joel H Ferziger, Milovan Perić, and Robert L Street. *Computational methods for fluid dynamics*.
547 Springer, 2019.
- 548 Konrad A Goc, Oriol Lehmkuhl, George Ilhwan Park, Sanjeeb T Bose, and Parviz Moin. Large
549 eddy simulation of aircraft at affordable cost: a milestone in computational fluid dynamics. *Flow*,
550 1:E14, 2021.
- 552 Gaurav Gupta, Xiongye Xiao, and Paul Bogdan. Multiwavelet-based operator learning for differen-
553 tial equations. *Advances in neural information processing systems*, 34:24048–24062, 2021.
- 554 Jayesh K Gupta and Johannes Brandstetter. Towards multi-spatiotemporal-scale generalized pde
555 modeling. *Transactions on Machine Learning Research*, 2023.
- 557 Zhou Hang, Yuezhou Ma, Haixu Wu, Haowen Wang, and Mingsheng Long. Unisolver: Pde-
558 conditional transformers are universal pde solvers. *arXiv preprint arXiv:2405.17527*, 2024.
- 559 Steeven Janny, Aurélien Beneteau, Madiha Nadri, Julie Digne, Nicolas Thome, and Christian Wolf.
560 Eagle: Large-scale learning of turbulent fluid dynamics with mesh transformers. *arXiv preprint*
561 *arXiv:2302.10803*, 2023.
- 563 George Karniadakis and Spencer J. Sherwin. *Spectral/HP Element Methods for Computational*
564 *Fluid Dynamics*. Oxford University Press, USA, 2005.
- 566 Dmitrii Kochkov, Jamie A Smith, Ayya Alieva, Qing Wang, Michael P Brenner, and Stephan
567 Hoyer. Machine learning–accelerated computational fluid dynamics. *Proceedings of the National*
568 *Academy of Sciences*, 118(21):e2101784118, 2021.
- 569 Zijie Li, Dule Shu, and Amir Barati Farimani. Scalable transformer for pde surrogate modeling.
570 *Advances in Neural Information Processing Systems*, 36, 2024.
- 571 Zongyi Li, Nikola Kovachki, Kamyar Azizzadenesheli, Burigede Liu, Kaushik Bhattacharya, An-
572 drew Stuart, and Anima Anandkumar. Fourier neural operator for parametric partial differential
573 equations. *arXiv preprint arXiv:2010.08895*, 2020.
- 574 Zichao Long, Yiping Lu, Xianzhong Ma, and Bin Dong. Pde-net: Learning pdes from data. In
575 *International conference on machine learning*, pp. 3208–3216. PMLR, 2018.
- 576 Zichao Long, Yiping Lu, and Bin Dong. Pde-net 2.0: Learning pdes from data with a numeric-
577 symbolic hybrid deep network. *Journal of Computational Physics*, 399:108925, 2019.
- 578 Lu Lu, Pengzhan Jin, Guofei Pang, Zhongqiang Zhang, and George Em Karniadakis. Learning
579 nonlinear operators via deepnet based on the universal approximation theorem of operators.
580 *Nature machine intelligence*, 3(3):218–229, 2021.
- 581 Yiping Lu, Aoxiao Zhong, Quanzheng Li, and Bin Dong. Beyond finite layer neural networks:
582 Bridging deep architectures and numerical differential equations. In *International Conference on*
583 *Machine Learning*, pp. 3276–3285. PMLR, 2018.
- 584 Fadl Moukalled, Luca Mangani, and Marwan Darwish. *The finite volume method in computational*
585 *fluid dynamics*. Springer, 2016.
- 586 Tobias Pfaff, Meire Fortunato, Alvaro Sanchez-Gonzalez, and Peter W Battaglia. Learning mesh-
587 based simulation with graph networks. *arXiv preprint arXiv:2010.03409*, 2020.
- 588 Md Ashiqur Rahman, Zachary E Ross, and Kamyar Azizzadenesheli. U-no: U-shaped neural oper-
589 ators. *arXiv preprint arXiv:2204.11127*, 2022.

- 594 Maziar Raissi, Paris Perdikaris, and George E Karniadakis. Physics-informed neural networks: A
595 deep learning framework for solving forward and inverse problems involving nonlinear partial
596 differential equations. *Journal of Computational physics*, 378:686–707, 2019a.
- 597
598 Maziar Raissi, Zhicheng Wang, Michael S Triantafyllou, and George Em Karniadakis. Deep learn-
599 ing of vortex-induced vibrations. *Journal of Fluid Mechanics*, 861:119–137, 2019b.
- 600
601 Maziar Raissi, Alireza Yazdani, and George Em Karniadakis. Hidden fluid mechanics: Learning
602 velocity and pressure fields from flow visualizations. *Science*, 367(6481):1026–1030, 2020.
- 603
604 Chengping Rao, Pu Ren, Yang Liu, and Hao Sun. Discovering nonlinear pdes from scarce data with
605 physics-encoded learning. *arXiv preprint arXiv:2201.12354*, 2022.
- 606
607 Chengping Rao, Pu Ren, Qi Wang, Oral Buyukozturk, Hao Sun, and Yang Liu. Encoding physics
608 to learn reaction–diffusion processes. *Nature Machine Intelligence*, 5(7):765–779, 2023.
- 609
610 Pu Ren, Chengping Rao, Yang Liu, Jian-Xun Wang, and Hao Sun. Phycrnet: Physics-informed
611 convolutional-recurrent network for solving spatiotemporal pdes. *Computer Methods in Applied
612 Mechanics and Engineering*, 389:114399, 2022.
- 613
614 Pu Ren, Chengping Rao, Yang Liu, Zihan Ma, Qi Wang, Jian-Xun Wang, and Hao Sun. Physr:
615 Physics-informed deep super-resolution for spatiotemporal data. *Journal of Computational
616 Physics*, 492:112438, 2023.
- 617
618 Yulia Rubanova, Ricky TQ Chen, and David K Duvenaud. Latent ordinary differential equations for
619 irregularly-sampled time series. *Advances in neural information processing systems*, 32, 2019.
- 620
621 Alvaro Sanchez-Gonzalez, Jonathan Godwin, Tobias Pfaff, Rex Ying, Jure Leskovec, and Peter
622 Battaglia. Learning to simulate complex physics with graph networks. In *International conference
623 on machine learning*, pp. 8459–8468. PMLR, 2020.
- 624
625 Xingjian Shi, Zhoung Chen, Hao Wang, Dit-Yan Yeung, Wai-Kin Wong, and Wang-chun Woo.
626 Convolutional lstm network: A machine learning approach for precipitation nowcasting. *Ad-
627 vances in neural information processing systems*, 28, 2015.
- 628
629 Xingjian Shi, Zhihan Gao, Leonard Lausen, Hao Wang, Dit-Yan Yeung, Wai-kin Wong, and Wang-
630 chun Woo. Deep learning for precipitation nowcasting: A benchmark and a new model. *Advances
631 in neural information processing systems*, 30, 2017.
- 632
633 Kimberly Stachenfeld, Drummond B Fielding, Dmitrii Kochkov, Miles Cranmer, Tobias Pfaff,
634 Jonathan Godwin, Can Cui, Shirley Ho, Peter Battaglia, and Alvaro Sanchez-Gonzalez. Learned
635 coarse models for efficient turbulence simulation. *arXiv preprint arXiv:2112.15275*, 2021.
- 636
637 Alasdair Tran, Alexander Mathews, Lexing Xie, and Cheng Soon Ong. Factorized fourier neural
638 operators. *arXiv preprint arXiv:2111.13802*, 2021.
- 639
640 Pantelis R Vlachas, Georgios Arampatzis, Caroline Uhler, and Petros Koumoutsakos. Multiscale
641 simulations of complex systems by learning their effective dynamics. *Nature Machine Intelli-
642 gence*, 4(4):359–366, 2022.
- 643
644 Rui Wang, Robin Walters, and Rose Yu. Incorporating symmetry into deep dynamics models for
645 improved generalization. *arXiv preprint arXiv:2002.03061*, 2020.
- 646
647 Yunbo Wang, Haixu Wu, Jianjin Zhang, Zhifeng Gao, Jianmin Wang, S Yu Philip, and Mingsheng
648 Long. Predrnn: A recurrent neural network for spatiotemporal predictive learning. *IEEE Trans-
649 actions on Pattern Analysis and Machine Intelligence*, 45(2):2208–2225, 2022.
- 650
651 Gege Wen, Zongyi Li, Kamyar Azizzadenesheli, Anima Anandkumar, and Sally M Benson. U-
652 fno—an enhanced fourier neural operator-based deep-learning model for multiphase flow. *Ad-
653 vances in Water Resources*, 163:104180, 2022.
- 654
655 Haixu Wu, Huakun Luo, Haowen Wang, Jianmin Wang, and Mingsheng Long. Transolver: A fast
656 transformer solver for pdes on general geometries. *arXiv preprint arXiv:2402.02366*, 2024.

648 Jiawei Zhuang, Dmitrii Kochkov, Yohai Bar-Sinai, Michael P Brenner, and Stephan Hoyer. Learned
649 discretizations for passive scalar advection in a two-dimensional turbulent flow. *Physical Review*
650 *Fluids*, 6(6):064605, 2021.
651
652 Olek C Zienkiewicz, Robert L Taylor, and Jian Z Zhu. *The Finite Element Method: Its Basis and*
653 *Fundamentals*. Elsevier, 2005.
654
655
656
657
658
659
660
661
662
663
664
665
666
667
668
669
670
671
672
673
674
675
676
677
678
679
680
681
682
683
684
685
686
687
688
689
690
691
692
693
694
695
696
697
698
699
700
701

702 APPENDIX

703 A IMPACT STATEMENT

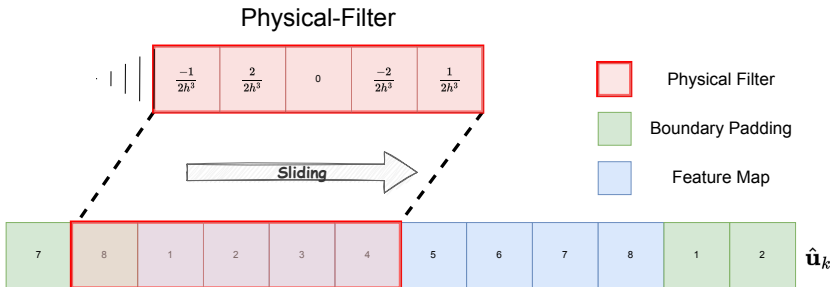
704
705 The paper endeavors to devise a adaptable framework that expedites simulations and predictive
706 analyses of physical systems by utilizing multi-scale temporal data. This framework harmoniously
707 integrates data-driven methodologies with physics-informed principles, striking a delicate balance
708 between empirical insights and theoretical underpinnings in its application. The framework can
709 be widely applied in various research fields including material science, turbulent flow prediction,
710 chemical engineering, and so forth. Our research is exclusively conducted for the pursuit of scientific
711 objectives and does not entail any potential ethical concerns or risks.

712 B DESIGN OF THE PHYSICAL FILTER

713
714 In the one-dimensional problem KdV, the original paper of PeRCNN did not provide the correspond-
715 ing model design. Following their concept, we present the corresponding physical filter.

$$716 f_{xxx} = \frac{-f_{i-2} + 2f_{i-1} + 0f_i - 2f_{i+1} + f_{i+2}}{2h^3} \tag{S1}$$

717
718 As shown in the Figure S1, we designed a Physical-Filter to represent $\frac{\partial^3 u}{\partial x^3}$ in the KdV equation. This



719
720
721
722
723
724
725
726
727
728
729
730
731
732
733
734 Figure S1: Filter for KdV

735 approach leverages the inherent physical properties of the system to accurately model the third-order
736 spatial derivative, thereby enhancing the accuracy and efficiency of the numerical solution. Among
737 the parameters, h indicates the Δx in the cases. The Boundary Padding is an approach to adapt
738 to periodic boundary conditions by replacing the original zero padding with a periodic boundary
739 padding.

740
741 C IMPLEMENTATION DETAILS

742 C.1 OVERVIEW

743 The overview of the PIMRL framework, which includes a pretraining stage using micro-scale data
744 for physics-informed Learning and the utilization of a micro-module, informed by learned physics
745 knowledge, to correct the macro-module during training on macro-scale data.

746
747 In the main body of this paper, we have elaborated on the architectures at the micro and macro
748 scales. Within the macro-scale module, there are components including an encoder, a decoder, and a
749 Residual Long Short-Term Memory (ResidualLSTM). The following section will provide a detailed
750 exposition of their configuration specifics.

751
752 C.2 ENCODER AND DECODER

753 In our framework, the autoencoder is employed not for the purpose of minimizing reconstruction
754 loss. Instead, the encoder is utilized to extract features, while the decoder serves to project the
755

756
757
758
759
760
761
762
763
764
765
766
767
768
769
770
771
772
773
774
775
776
777
778
779
780
781
782
783
784
785
786
787
788
789
790
791
792
793
794
795
796
797
798
799
800
801
802
803
804
805
806
807
808
809

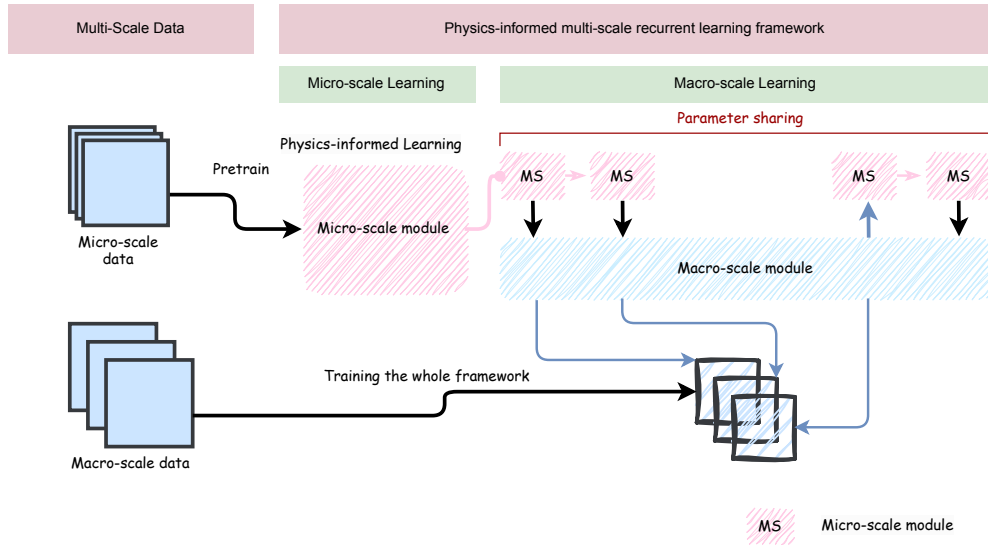


Figure S2: Overview of the PIMRL framework, which includes a pretraining stage using micro-scale data for physics-informed Learning and the utilization of a micro-module, informed by learned physics knowledge, to correct the macro-module during training on macro-scale data.

output of ConvLSTM into the physical space as residuals. The primary goal of the autoencoder in this context is to map an input to a low-dimensional latent space, and subsequently decode it to the original dimension at the output, facilitating the feature extraction and residual projection processes in the framework.

C.3 RESIDUALLSTM

The structure of ResidualLSTM has been clearly illustrated in the main text. Here, we will elucidate the architecture of the ConvLSTMcell as the Figure S3.

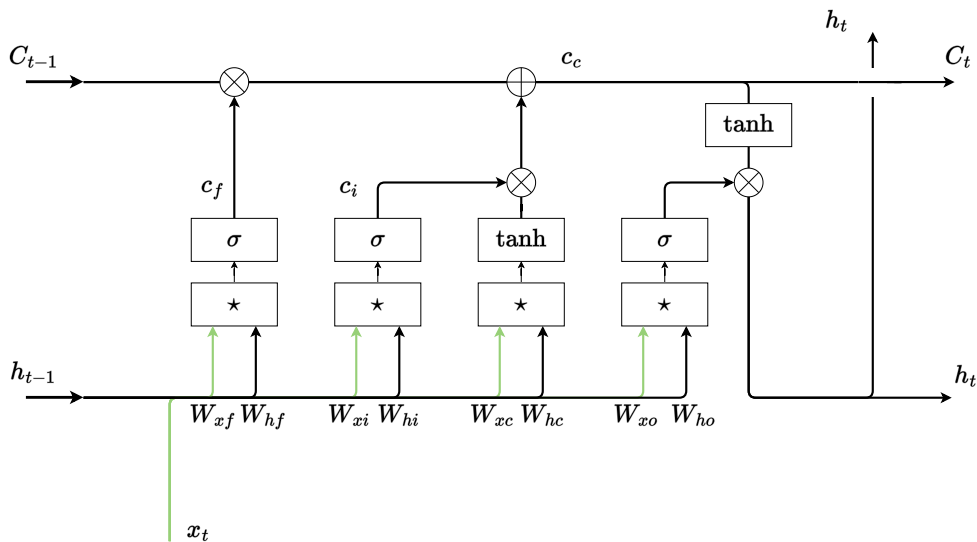


Figure S3: ConvLSTMCell

810
811
812
813
814
815
816
817
818
819
820
821
822
823
824
825
826
827
828
829
830
831
832
833
834
835
836
837
838
839
840
841
842
843
844
845
846
847
848
849
850
851
852
853
854
855
856
857
858
859
860
861
862
863

$$\begin{aligned}
 c_i &= \sigma(\mathbf{W}_{xi}(x_t) + \mathbf{W}_{hi}(h_{t-1})) \\
 c_f &= \sigma(\mathbf{W}_{xf}(x_t) + \mathbf{W}_{hf}(h_{t-1})) \\
 c_c &= c_f \cdot c + c_i \cdot \tanh(\mathbf{W}_{xc}(x_t) + \mathbf{W}_{hc}(h_{t-1})) \\
 C_t &= \sigma(\mathbf{W}_{xo}(x_t) + \mathbf{W}_{ho}(h_{t-1})) \\
 h_t &= c_o \cdot \tanh(c_c)
 \end{aligned}
 \tag{S2}$$

The set of equations S2 presented above outlines the operations of a ConvLSTM cell. The equations involve computations of various gates and states within the cell, including input gate c_i , forget gate c_f , cell state c_c , output C_t , and the updated hidden state h_t . These equations govern the flow of information and transformations within the ConvLSTM cell, enabling the model to process spatiotemporal data efficiently by considering spatial dimensions in the calculations. The parameters W_{xi} , W_{hi} , W_{xf} , W_{hf} , W_{xo} , and W_{ho} , depicted in Figure S3, manage information from inputs (x_t) and history (h_{t-1}, C_{t-1}) in a convolutional manner.

D BASELINE MODELS

In order to compare and evaluate the performance of our proposed method, we have trained multiple state-of-the-art (SOTA) baseline models as well as classical models, and compared them with our model. The introductions to each baseline model are presented below, while the training details are outlined in subsequent sections E.

Fourier Neural Operator (FNO). FNOLi et al. (2020) is a method that combines Fourier transforms with neural networks. This approach comprises two main components. The first component involves performing Fourier transforms on the system state quantities, learning certain information in the frequency domain, and then applying an inverse transform. The second component utilizes convolutions to process the system state quantities, complementing the information not captured during the frequency domain learning. The combination of these two components serves as the final result. We make two FNO models sharing the same architecture, which training in micro and macro scale datasets respectively and inferring in micro and macro time intervals. In the same model, we conducted training separately for two types of data, resulting in FNO and FNO-coarse.

ConvLSTM. ConvLSTM (Shi et al., 2015) is a specialized neural network architecture that combines convolutional and LSTM layers to effectively model spatial and temporal dependencies in sequential data.

PeRCNN. PeRCNN (Rao et al., 2023) represents a physics-informed learning methodology, embedding physical laws directly into the neural network architecture. It incorporates multiple parallel convolutional neural networks (CNNs), leveraging the simulation of polynomial equations through feature map multiplication. By doing so, PeRCNN augments the model’s extrapolation and generalization capabilities.

E TRAINING DETAILS

All experiments were conducted on a single 80GB Nvidia A100 GPU, using an Intel(R) Xeon(R) Platinum 8380 CPU (2.30GHz, 64 cores). We only give some of the changed parameters here, and the other hyperparameters remain the same as the original text.

PIMRL. The architecture of the PIMRL model, illustrated in Figure 3, utilizes the Adam optimizer with a learning rate of 5×10^{-3} . The model have different parameters in different cases. More details were given by Table S2.

Additionally, we implement the StepLR scheduler to adjust the learning rate by a factor of 0.98 every 200 epochs. The pretraining details is same to the baseline model PeRCNN.

FNO and FNO-coarse. The network structure of FNO remains largely in line with the original study, with the primary adjustment being the adoption of an autoregressive training method for this model. We employ the Adam optimizer with a learning rate of 1×10^{-3} . More details are shown in the Table S8 and Table S9.

ConvLSTM. For ConvLSTM, we implement the ConvLSTM architecture like the macro-scale module of PIMRL. The StepLR scheduler is utilized with a step size of 200 and a gamma value of 0.98. The optimizer of choice is Adam, featuring a learning rate set at 1×10^{-3} . More details are shown in the Table S10.

PeRCNN. For PeRCNN, the training is different from the original paper since the micro-scale data only get a few pairs of continuous data. It is impossible to train PeRCNN in 400 to 800 steps at the same time. The details were shown in Table S5. We employ the Adam optimizer with learning rate of 1×10^{-3} and the StepLR scheduler to adjust the learning rate by a factor of 0.98 per 200 epochs.

F EVALUATION METRICS

In this paper, we have adopted some classical evaluation metrics such as RMSE, MAE and HCT. Root Mean Square Error (RMSE) quantifies the average error magnitude between estimated and actual values, serving as a gauge of the model’s precision. Conversely, Mean Absolute Error (MAE) assesses the average absolute disparity between anticipated and observed values, denoting the true scale of discrepancies.

The definitions of these metrics are as follows:

$$\begin{aligned} \text{RMSE (Root Mean Square Error):} & \sqrt{\frac{1}{n} \sum_{i=1}^n (y_i - \hat{y}_i)^2} \\ \text{MAE (Mean Absolute Error):} & \frac{1}{n} \sum_{i=1}^n |y_i - \hat{y}_i| \\ \text{HCT (High Correction Time):} & \sum_{i=1}^N \Delta t \cdot 1(\text{PCC}(y_i, \tilde{y}_i) > 0.8) \end{aligned} \quad (\text{S3})$$

In the above equations S3, n represents the number of trajectories, y_i represents the true value, and \hat{y}_i represents the predicted value of the model. The PCC is the Pearson correlation coefficient, which is a statistical metric used to measure the linear correlation between two variables.

G DATASET INFORMATIONS

The IC for the Kdv equation is created by summing multiple sine waves with random amplitudes, phases, and frequencies, resulting in a complex waveform. Initial conditions for the Burgers’ equation are generated randomly according to a Gaussian distribution. The FN equation is initialized with random Gaussian noise for a warm-up period, after which time sequences are extracted to form the dataset. The GS equation starts the reaction from random initial positions then diffuses.

Table S1: Summary of experimental settings for different cases.(The 3D GS case is downsampled from 96^3 to 48^3 during training)

Case	Numerical Methods	Spatial Grid	Time Grid	Training Trajectories	Test Trajectories
Kdv	FVM	256	0.01s	5	2
Burgers	FDM	128^2	0.001	13	3
FN	FDM	128^2	0.5	5	3
2DGS	FDM	128^2	0.002	2	3
3DGS	FDM	96^3	0.25	3	2

Korteweg-de Vries Equation. The Korteweg-de Vries system, which elucidates the evolution of waves in nonlinear wave phenomena, can be described by the equation:

$$\frac{\partial u}{\partial t} = -u \frac{\partial u}{\partial x} - \frac{\partial^3 u}{\partial x^3} \quad (\text{S4})$$

We got the 8 sets of data: 5 for training, 1 for validation, and 2 for testing. The data sets had spatial domain size $x \in [0, 64]$, where Δt is 15 times δt and $\delta t = 0.01s$.

2D Burgers Equation. The 2D Burgers' equation is commonly employed as a benchmark model for comparing and evaluating different computational algorithms, and describes the complex interaction between nonlinear convection and diffusion processes in the way like:

$$\frac{\partial u}{\partial t} = -uu_x - vv_y + \nu(u_{xx} + u_{yy}), \quad (S5)$$

$$\frac{\partial v}{\partial t} = -uv_x - vv_y + \nu(v_{xx} + v_{yy}). \quad (S6)$$

The u_t and v_t is the fluid velocities and ν denotes the viscosity coefficient. In this case, we choose $\nu = 0.005$ and the spatial domain size $x \in [0, 1]$, where Δt is 8 times δt and $\delta t = 0.001s$.

2D FitzHugh-Nagumo Equation.The FitzHugh-Nagumo system can be described by the equation:

$$\frac{\partial u}{\partial t} = \mu_u \Delta u + u - u^3 - v + \alpha, \quad (S7)$$

$$\frac{\partial v}{\partial t} = \mu_v \Delta v + (u - v)\beta. \quad (S8)$$

The coefficients $\alpha = 0.01$ and $\beta = 0.25$, governing the reaction process, take distinct values, while the diffusion coefficients are $\mu_u = 1$ and $\mu_v = 100$. In terms of time, $\Delta t = 15\delta t$ and $\delta t = 0.002s$.

2D and 3D Gray-Scott Equation. The Gray-Scott equations describe the temporal and spatial variations of chemical concentrations in reaction-diffusion systems, which can be described by the equation:

$$\frac{\partial u}{\partial t} = D_u \nabla^2 u - uv^2 + F(1 - u), \quad (S9)$$

$$\frac{\partial v}{\partial t} = D_v \nabla^2 v + uv^2 - (F + k)v. \quad (S10)$$

Here, in the two-dimensional case, D_u and D_v represent the diffusion coefficients of the two substances, with specific values of $D_u = 2.0 \times 10^{-5}$ and $D_v = 5.0 \times 10^{-6}$. $F = 0.04$ denotes the growth rate of the substance, while $k = 0.06$ signifies its decay rate. In the 2D Gray-Scott case, we got 5 trajectories for training, 1 trajectory for validation and 3 trajectories for testing, where $\Delta t = 15\delta t$ and $\delta t = 0.5s$. In the three-dimensional case, we have the parameters: $DA = 0.2$, $DB = 0.1$, $F = 0.025$, and $k = 0.055$. We got 3 trajectories for training, 1 trajectory for validation and 2 trajectories for testing, where $\Delta t = 15\delta t$ and $\delta t = 0.25s$.

Table S2: Training Details of PIMRL.

Case	Batchsize	Num of epochs
KdV	512(all)	5000
Burgers	8	5000
2DGS	4	5000
FN	32	8000
3DGS	16	8000

H SUPPLEMENT RESULTS

972
973
974
975
976
977
978
979
980
981
982
983
984
985
986
987
988
989
990
991
992
993
994
995
996
997
998
999
1000
1001
1002
1003
1004
1005
1006
1007
1008
1009
1010
1011
1012
1013
1014
1015
1016
1017
1018
1019
1020
1021
1022
1023
1024
1025

Table S3: The Result of U-NO, F-FNO, MWT and FNO in the FN Case.

Metrics	U-NO	F-FNO	MWT	FNO
RMSE	0.3675	0.2280	0.3494	0.1878
MAE	0.1465	0.1350	0.2228	0.1634

Table S4: Results with Error Bar under RMSE metric on all Cases.

Model	PIMRL	PeRCNN
Kdv	0.0457 ± 0.0053	0.0942 ± 0.0082
Burgers	0.0068 ± 0.0006	0.0075 ± 0.0008
2DGS	$0.0133 \pm 2.4 \times 10^{-12}$	$0.0455 \pm 1.9 \times 10^{-11}$
FN	0.1349 ± 0.0040	0.1591 ± 0.0061
3DGS	0.0381 ± 0.0015	0.0532 ± 0.0027

Table S5: Training Details of PeRCNN.

Case	Batchsize	Num of epochs	Steps
KdV	512(all)	1000	45
Burgers	32	1000	16
2DGS	32	1000	45
FN	36	1000	45
3DGS	32	1000	45

Table S6: Comparison of RMSE and MAE for different cases.

Case	RMSE	MAE
FN	0.2803	0.2482
2DGS	NaN	NaN

Table S7: Running Time, Parameter Size, and GPU Memory for PIMRL, U-NO, MWT, FNO, and ConvLSTM

Model	Running Time	Parameter Size	GPU Memory
PIMRL	9 s	3.33 M	1728 M
U-NO	7 s	15.29 M	2320 M
MWT	12 s	0.09 M	1732 M
FNO	2 s	8.39 M	1580 M
ConvLSTM	5 s	3.32 M	1708 M

Table S8: Training Details of FNO.

Case	Batchsize	Num of epochs	Steps
KdV	512(all)	1000	45
Burgers	32	2000	16
2DGS	32	2000	45
FN	36	2000	45
3DGS	32	2000	45

1026
1027
1028
1029
1030
1031
1032
1033
1034
1035
1036
1037
1038
1039
1040
1041
1042
1043
1044
1045
1046
1047
1048
1049
1050
1051
1052
1053
1054
1055
1056
1057
1058
1059
1060
1061
1062
1063
1064
1065
1066
1067
1068
1069
1070
1071
1072
1073
1074
1075
1076
1077
1078
1079

Table S9: Training Details of FNO-coarse.

Case	Batchsize	Num of epochs
KdV	512(all)	5000
Burgers	32	5000
2DGS	32	5000
FN	32	8000
3DGS	16	8000

Table S10: Training Details of ConvLSTM.

Case	Batchsize	Num of epochs
KdV	512(all)	5000
Burgers	8	5000
2DGS	4	5000
FN	32	8000
3DGS	16	8000